3-D Printed Non-Interleaved Reflective Metasurfaces Supporting Dual-Band Spin-Decoupled Quadruplex Channel Independent Beam-Shaping With Controllable Energy Distribution

Jianfeng Zhu, *Member, IEEE*, Yang Yang, *Senior Member, IEEE,* Jiexin Lai, *Student Member, IEEE*, Mengze Li, *Student Member, IEEE*

Abstract—This article presents 3-D printed non-interleaved reflective metasurfaces (MSs), which support millimeter-wave (mm-wave) dual-band spin-decoupled quadruplex channels with independent beam-shaping. The MS's unit cell (UC) is made of a cross-bar structure mounted on a circular-shaped patch antenna, which connects to short-ended time delay lines (TDLs). Pancharatnam-Berry (P-B) and dynamic phases are used to decouple the two spin states. Specifically, rotating the top cross-bar structure and adjusting its size provides the high-band's P-B and dynamic phases. Rotating the circular patch antenna and adjusting the length of the TDL introduce the P-B phase and dynamic phase for the low band, respectively. In addition, the mutual interference between the dual bands is minimal. The size of the non-interleaved UC is only 4 mm, corresponding to 0.33 and 0.48 free space wavelength of the center frequency for low-band (25-GHz) and high-band (36-GHz), respectively. For proof of concept, an MS generating orbit angular momentum (OAM) with different topological charges in four channels is fabricated and measured. Furthermore, in addition to the independent wavefront shaping, the energy distribution ratio in the reflected co-pol and cross-pol channels can also be independently controlled over dual-band under a circularly polarized incident wave. An MS, which generates near-field focusing with different energy distributions ratio in dual bands, is fabricated and experimentally verified for demonstration. The MS samples are prototyped using a multi-material 3-D printing technique on a single substrate.

Index Terms—3-D printing, dual-band, energy distribution, metasurface, multiplexing, spin-decoupled.

I. INTRODUCTION

METASURFACES (MSs) are composed of two-dimensional periodic subwavelength metal/dielectric unit cells (UCs) that can manipulate the amplitude, phase, and
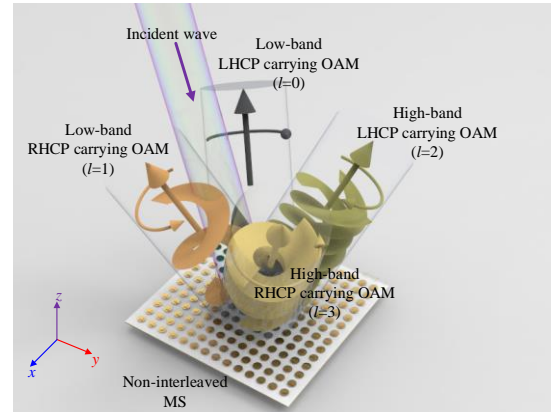

Fig. 1. Basic configuration of the dual-band spin-decoupled non-interleaved MS for multi-mode OAM generation.

polarization states of the electromagnetic (EM) wave in the desired manners [1], [2], [3], [4], [5], [6], [7], [8], [9], [10], [11], [12], [13], [14], [15]. Unlike conventional devices where phase accumulation depends on wave propagation, MSs generate strong light-matter interaction to produce abrupt phase change with ultrathin thickness [16], [17], [18]. Pancharatnam–Berry (P-B) phase is one of the common methods to manipulate the phase of the circularly polarized wave by simply rotating the half-wave plate (HWP) based UC [19], [20], [21], [22], [23]. The phase-shifting for the two spin states, *i.e.*, the left-hand circularly polarization (LHCP) and the right-hand circularly polarization (RHCP) waves, show opposite tendencies. The absolute phase-shifting values are twice the rotation angles. By combing the dynamic phase and P-B phase, LHCP and RHCP can be fully decoupled, paving the way to the high-efficient polarization-multiplexed communication system [24], [25], [26], [27], [28], [29], [30], [31], [32], [33], [34]. Signal multiplexing methods are widely used in microwave and optical wireless communications, including space, angle, polarization, frequency, and orbital angular momentum multiplexing. Traditional systems require source coding and physical circuits to implement these multiplexing, which complicates the hardware design and software. The MS-enabled space-frequency-polarization-division multiplexed modulations have been recognized as a new architecture to improve channel capacity and space

utilization [35], [36]. The popular strategy in the literature to achieve frequency-polarization multiplexed function use either interleaved elements or stacking multiple structures with frequency-selective-surface (FSS) in between. For example, the frequency and wavevector multiplexed spin-decoupled MSs were reported by interleaving split rings and cross-bar structures [37]. K-/Ka dual band spin decoupled reflectarray was reported by interleaving two different patch antennas connected with microstrip phase delay lines [38]. However, interleaved configuration usually results in the large size of the UC, which restricts the MS's performance, e.g., beam steering angle. In addition, too small a UC may give rise to strong mutual interference between the dual bands. To eliminate the mutual interference, stacking UCs in different layers with FSS between them can be a good choice [39],[40]. For example, spin-decoupled reflectarray independently operating at Ku / Ka dual-band was reported by using double-layer FSS [40]. However, these MSs with stacked configurations need at least three printed circuit board (PCB) laminates, which require a complicated and time-consuming manual assembly process and alignment, making industrial-level mass production and mounting a real challenge. Recently, a non-interleaved MS achieving dual-band dual CP holographic images was demonstrated [41]. Nevertheless, only 1-bit resolution is adopted to implement the UC. Meanwhile, state-of-the-art reflective MSs mainly focus on the co-polarization channel beam-shaping due to the nature of the P-B phase. However, a cross-polarization channel is inevitable when the UC does not function as a perfect HWP. Actually, it is desirable that the MS functions as an energy route [42], which can redistribute input energy to co-polarization and cross-polarization channels and independently shape their wavefronts simultaneously.

As for fabrication, most state-of-the-art microwave MSs are fabricated using PCB. Though PCB is a mature technology, it is not cost-effective to fabricate some sophisticated structures, such as multi-layered designs with penetrating vias. Usually, an additional bonding technique is required to provide a robust connection between layers. The conductor and dielectric joint 3-D printing technique was recently demonstrated to address these issues, providing the designer with more flexibility [43],[44]. The multi-layered MS can be printed with fewer constraints, especially the number of layers and the distance between adjacent layers. In addition, the one-stop printing enables the MS to be fast prototyped in an additive way rather than subtracting manner with less cost and waste.

This article presents 3-D printed non-interleaved reflective millimeter-wave (mm-wave) MSs for dual-band spin-decoupled quadruplex channel with independent beam-shaping. A schematic illustration of the MS function is shown in Fig. 1. The MS's UC is made of a cross-bar structure mounted on a circular-shaped patch antenna that connects to time delay lines (TDLs). Because of the unique structure of the UC, the mutual interference between the dual bands is minimal. Therefore, P-B and dynamic phases can be applied to both bands to decouple the spin states simultaneously. For
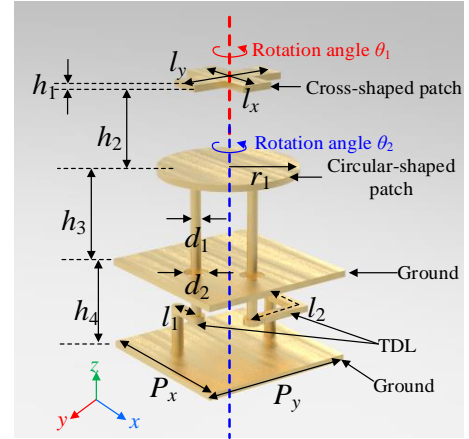

Fig. 2. Configuration and dimensions of the UC. (Not scaled in the z-direction). h_1=0.035mm, h_2=0.43 mm, h_3=0.535 mm, h_4=0.5 mm, r_1=1.7 mm, d_1=0.26 mm, d_2=0.6 mm, P_x=4 mm, P_y=4 mm.

proof of concept, MS that generates orbital angular momentum (OAM) with different topological charges in frequency-polarization multiplexed channels is fabricated and measured first. Then, in addition to the independent wavefront shaping, an MS, which generates near-field focusing with controllable energy distributions in the reflected co-polarization and cross-polarization over dual-band under LHCP incident wave, is fabricated and experimentally verified. The MS samples are prototyped by using the conductor and dielectric joint multi-material 3-D printing technique.

II. METASURFACE FOR QUADRUPLEX CHANNEL INDEPENDENT BEAM-SHAPING

A. Meta-Atom Design and Principle

The configuration of the UC is shown in Fig. 2, which consists of five conductor layers (35 μm, h_1) with a total thickness of 1.5mm, corresponding to 0.125 free space wavelength at 25 GHz. The conductor layers are implemented by nanoparticle silver ink, and the dielectric layer is implemented using ultraviolet (UV) curable acrylates ink (dielectric constant=2.8, loss tangent=0.012). An anisotropic cross-bar structure is mounted on the top of the circular-shaped patch antenna. The cross-bar structure is resonant at the high-band (center frequency: 36 GHz). Thus, the dynamic phase can be achieved by varying the patch size. Meanwhile, rotating the cross-bar structure (θ_1) introduces P-B phase in the high band. Thus, the LHCP and RHCP beams can be decoupled by combining the two uncorrelated phase-shifting methods. Note the circular-shaped patch antenna functions as the ground of the cross-bar structure in the high band. In contrast, the circular-shaped dual-polarized patch antenna receives the EM-wave in the low-band (center frequency: 25 GHz) and induces it into the TDLs, which are shorted to the bottom ground. Then, the energy is reflected and re-radiated into the free space. Hence, LHCP and RHCP in the low-band can be decoupled by adjusting the TDLs' length (dynamic phase) and rotating the patch antenna and the TDLs (θ_2, P-B phase). It is worth mentioning that though different structures
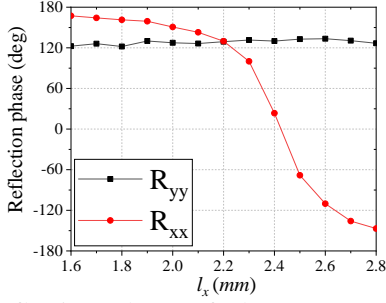
Fig. 3. Reflection phase of the meta-atom along x-polarization and y-polarization at 25 GHz with different values of l_x. (l_y is fixed at 2.2 mm)

can implement patch antenna, the circular-shaped patch is adopted because of its rotation symmetry feature. In other words, the possible effects on the high-band due to the rotation of the patch can be minimal since the circular ground is rotation symmetry. The size of the meta-atom is only 4 mm along the x- and y-direction, corresponding to 0.33 and 0.48 free space wavelength of center frequency for low-band (25-GHz) and high-band (36-GHz), respectively.

To independently manipulate the LHCP ($|L\rangle=[1\ i]/\sqrt{2}$) and RHCP ($|R\rangle=[1\ -i]\ /\ \sqrt{2}$), the MS should provide two uncorrelated phase profiles, namely, $\varphi_L(x,y)$ for LHCP and $\varphi_R(x,y)$ for RHCP. For the LHCP and RHCP input, we can design a birefringent surface where the output polarization state can be $|R\rangle^*$ and $(|L\rangle^*$, where * denotes the complex conjugate of input polarization states. Therefore, the original system can be expressed as [31]:

$$J(x,y)\begin{bmatrix}1\\i\end{bmatrix}=e^{i\varphi_L(x,y)}\begin{bmatrix}1\\-i\end{bmatrix} \quad \text{for LHCP} \quad (1)$$

$$J(x,y)\begin{bmatrix}1\\-i\end{bmatrix}=e^{i\varphi_R(x,y)}\begin{bmatrix}1\\i\end{bmatrix} \quad \text{for RHCP}. \quad (2)$$

Combining (1) and (2), the Jones Matrix can be expressed as:

$$J(x,y)=\frac{1}{2}\begin{bmatrix}e^{i\varphi_L(x,y)}+e^{i\varphi_H(x,y)} & ie^{i\varphi_R(x,y)}-ie^{i\varphi_L(x,y)}\\ie^{i\varphi_R(x,y)}-ie^{i\varphi_L(x,y)} & -e^{i\varphi_L(x,y)}-e^{i\varphi_R(x,y)}\end{bmatrix}. \quad (3)$$

Then, the Jones matrix $J(x,y)$ can be decomposed into the canonical form [31]:

$$J(x,y)=P\Lambda P^{-1}=$$

$$\begin{bmatrix}\cos\frac{1}{4}[\varphi_L(x,y)-\varphi_R(x,y)] & -\sin\frac{1}{4}[\varphi_L(x,y)-\varphi_R(x,y)]\\\sin\frac{1}{4}[\varphi_L(x,y)-\varphi_R(x,y)] & \cos\frac{1}{4}[\varphi_L(x,y)-\varphi_R(x,y)]\end{bmatrix}\cdots$$

$$\begin{bmatrix}e^{i[\frac{1}{2}(\varphi_L(x,y)+\varphi_R(x,y))]} & 0\\0 & e^{i[\frac{1}{2}(\varphi_L(x,y)+\varphi_R(x,y))]-\pi}\end{bmatrix}\cdots$$

$$\begin{bmatrix}\cos\frac{1}{4}[\varphi_L(x,y)-\varphi_R(x,y)] & -\sin\frac{1}{4}[\varphi_L(x,y)-\varphi_R(x,y)]\\\sin\frac{1}{4}[\varphi_L(x,y)-\varphi_R(x,y)] & \cos\frac{1}{4}[\varphi_L(x,y)-\varphi_R(x,y)]\end{bmatrix}^{-1}. \quad (4)$$

Here, P can be regarded as a rotation matrix for the matrix Λ. Thus, the dynamic phase-shifting and the rotation angle of the UC (θ) can be calculated as:
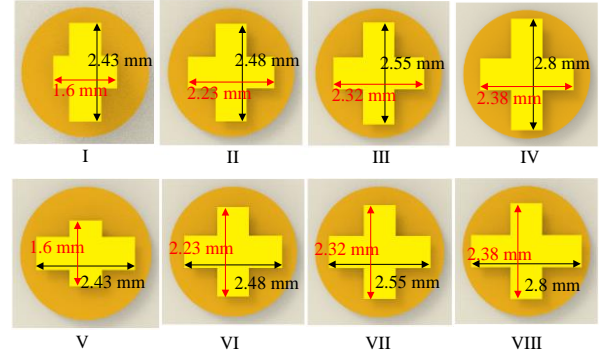

Fig. 4. Configuration of the eight-level cross-bar structure for high-band spin-decoupling.

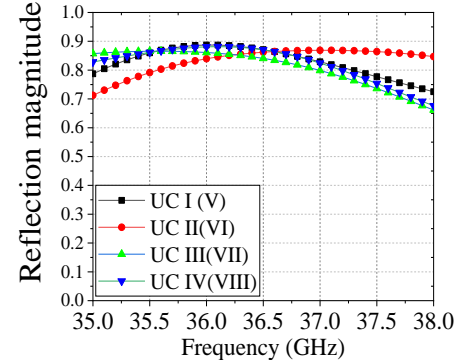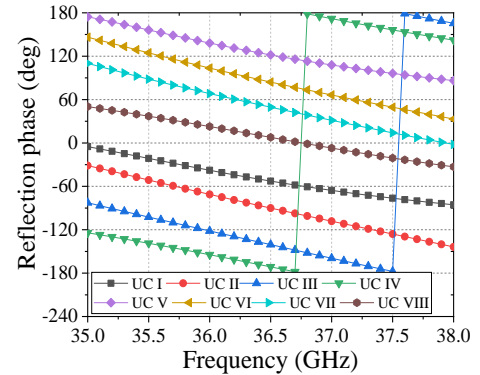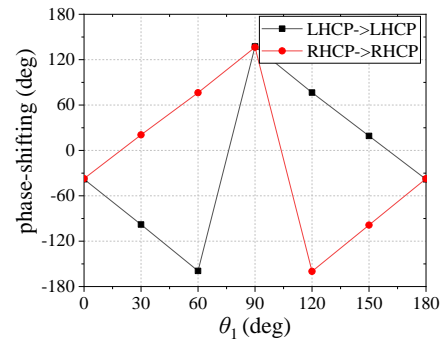**Fig. 5.** Reflection magnitudes of the eight-level UCs for high-band spin-decoupling.

$$\delta_x(x,y)=[\varphi_L(x,y)+\varphi_R(x,y)]/2 \quad (5)$$

(a)

(b)

Fig. 6. (a) Reflection phases of the eight-level UCs. (b) Co-polarization reflection phase of UC I at 36 GHz.
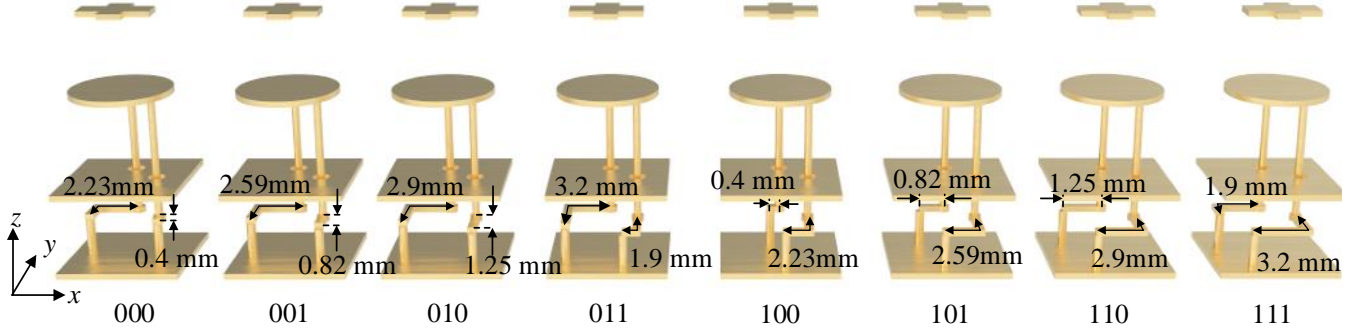
Fig. 7. Eight-level UC with different lengths of TDLs to achieve low-band spin-decoupling. (Not scaled in the z-direction)
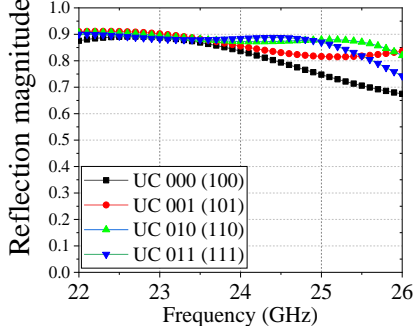

Fig. 8. Reflection magnitudes of the eight-level UCs.

$$\delta_y(x, y) = [\varphi_L(x, y) + \varphi_R(x, y)]/2 - \pi \qquad (6)$$

$$\theta(x, y) = [\varphi_L(x, y) - \varphi_R(x, y)]/4 \quad . \qquad (7)$$

This requires the UCs to provide π phase retardation between the x and y-polarized incident waves and provide dynamic phase covering 2π phase-shifting to achieve the independent
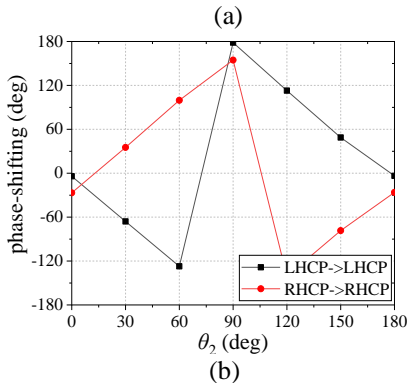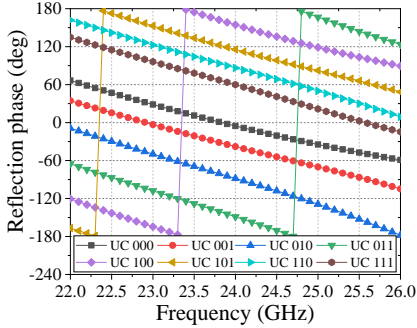
manipulation of the LHCP and RHCP.

Numerical simulation is carried out to verify the meta-atom. The reflection phase at the high-band by varying the length of the cross-shaped patch (l_x) along the x-direction is given in Fig. 3. It is seen that more than 320° phase-shifting can be achieved for the reflected x-polarized channel (R_{xx}) by adjusting l_x from 1.6 mm to 2.8 mm while phase-shifting for the reflected y-polarized channel (R_{yy}) is near constant. Therefore, an eight-level UC is designed to achieve high-band spin-decoupling. Their dimensions are given in Fig. 4. The co-polarization reflection magnitudes of the eight-level UC under CP incident wave are shown in Fig. 5. The co-polarization reflection magnitudes are between 0.8 to 0.9 over most of the band. The co-polarization reflection phases of the eight-level UC are shown in Fig. 6 (a), which covers the required 2π dynamic phase shifting. Note that the dimensions of element V (VI/VII/VIII) are the same as element I (II/III/IV), but rotated with an angle of 90°. Therefore, their reflection

(a)

(b)

Fig. 9. (a) Reflection phases of the eight-level UCs. (b) Co-polarization reflection phase at 25 GHz.
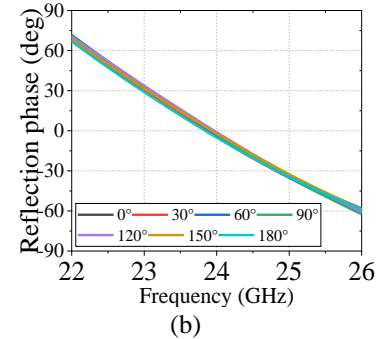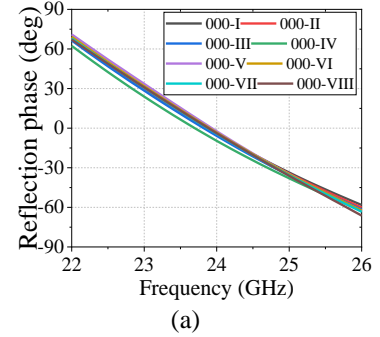

(a)

(b)

Fig. 10. (a) Reflection phases of UC (000) in low-band when the size of the cross-bar structure is varied. (b) Reflection phases of UC (000) in low-band when the cross-bar structure is rotated.
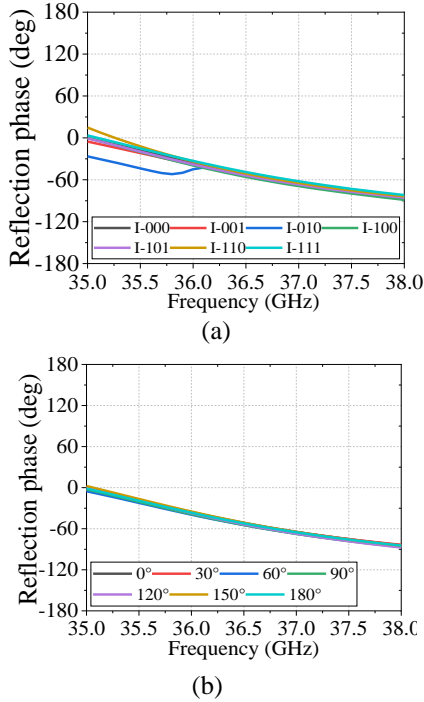
Fig. 11. (a) Reflection phases of UC (I) in high-band when TDL's length is varied. (b) Reflection phases of UC (I) in high-band when the circular patch antenna is rotated.

Fig. 12. Phase masks for the quadruplex channels.

Fig. 11 (a) shows the reflection phase at the high band when the lengths of the TDLs are varied from 000 to 111. The maximum reflection phase difference between curves is less than 35°. Meanwhile, rotating the antenna in the bottom does not affect the high-band phase-shifting, as shown in Fig. 11 (b). Therefore, the size and rotation angles of the cross-bar and patch antenna can be independently adopted to decouple the LHCP and RHCP in high-band and low-band, respectively.

magnitudes are the same, but the phase-shifting value has a 180° difference due to the P-B phase. The co-polarization reflection phase when UC I is rotated is given in Fig. 6 (b). The phase-shifting of the reflected co-polarization channels under RHCP and LHCP incident waves show opposite tendencies, and the absolute values are twice the rotation angle.

As for the low band, dynamic phase-shifting is achieved by adjusting the length of TDLs. Eight-level UCs, marked as 000 to 111, are designed for low-band spin-decoupling. Their dimensions are given in Fig. 7. The co-polarization reflection magnitudes of the eight-level UC under the CP incident wave in the low band are shown in Fig. 8. The co-polarization reflection magnitudes are above 0.8 over most of the band. The reflection performance is stable in both bands when the incident angles increase up to 30-degree. The co-polarization reflection phases of the eight-level UC are shown in Fig. 9 (a), which satisfies 2π dynamic phase shifting. Again, the dimensions of element 100 (101/110/111) are the same as element 000 (001/010/011), but rotated with an angle of 90°. Therefore, their reflection magnitudes are the same, but the phase-shifting value has a 180° difference due to the P-B phase. The co-polarization reflection phase when UC 000 is rotated is given in Fig. 9 (b). The phase-shifting of the reflected co-polarization channels reveals an opposite tendency, and the absolute values are equal to twice the rotation angle. Then, the mutual interference between the dual-band is investigated. Fig. 10 (a) shows the reflection phase at the low band when the cross-bar structure's size varies from I to VI. The reflection phase in the low-band is nearly constant regardless of the size of the top cross-bar structure. Meanwhile, rotating the cross-bar structure does not affect the low-band phase-shifting, as shown in Fig. 10 (b).
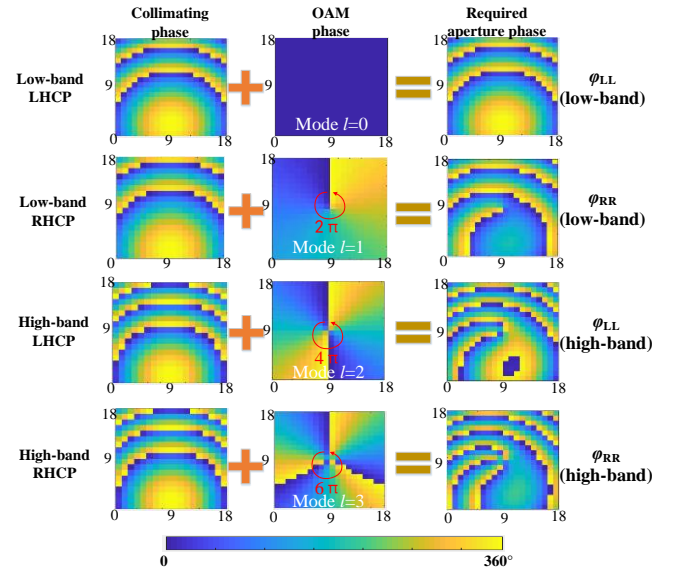

Fig. 13. (a) Phase mask for the low-band. (b) Phase mask for the high-band.

Fig. 14. MS under printing.

(a)   (b)

Fig. 15. (a) Top view of the MS. (b) Assembling view of the MS.

B. Metasurface Design and Results.

The MS is designed to collimate the EM wave from the feed and generate OAM with different topological charges for the LHCP and RHCP incident waves in low-band and high-band, respectively. The feed position is located at (x=-30mm, y=0mm, and z=70mm). To collimate the spherical wave from the feed and generate OAM simultaneously, the phase profile of R_{LL}, R_{RR} in low-band and high-band can be respectively expressed as:

$$R_{LL}(x, y) = k \cdot R_i + l \cdot \varphi (l = 0) \quad \text{for low-band (8)}$$
$$R_{RR}(x, y) = k \cdot R_i + l \cdot \varphi (l = 1) \quad \text{for low-band (9)}$$

Fig. 16. The measurement setup (d is set as 120 mm).

Fig. 17. Simulated and measured near-field intensity and phase. (Intensity is in dB scale)

$$R_{LL}(x, y) = k \cdot R_i + l \cdot \varphi (l = 2) \quad \text{for high-band (10)}$$
$$R_{RR}(x, y) = k \cdot R_i + l \cdot \varphi (l = 3) \quad \text{for high-band (11)}$$

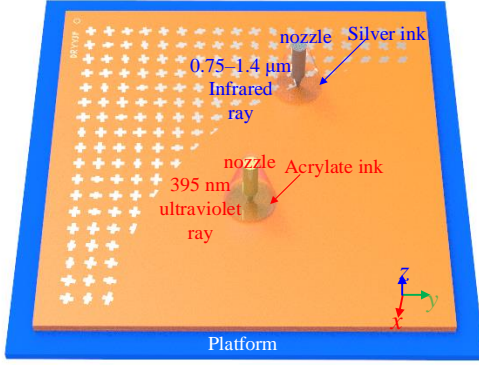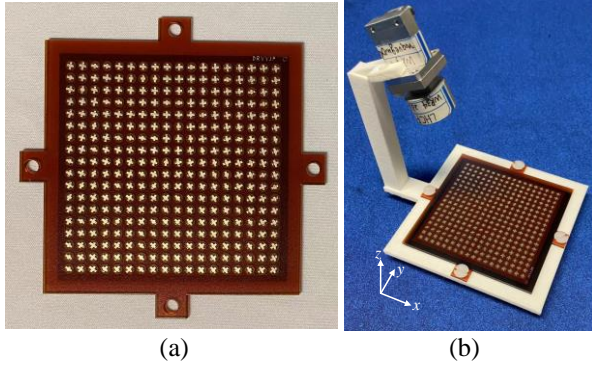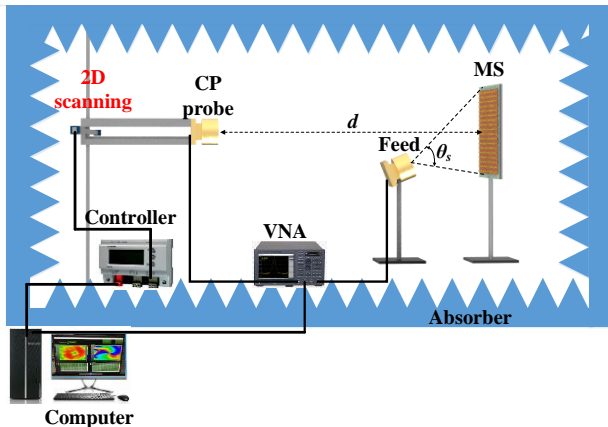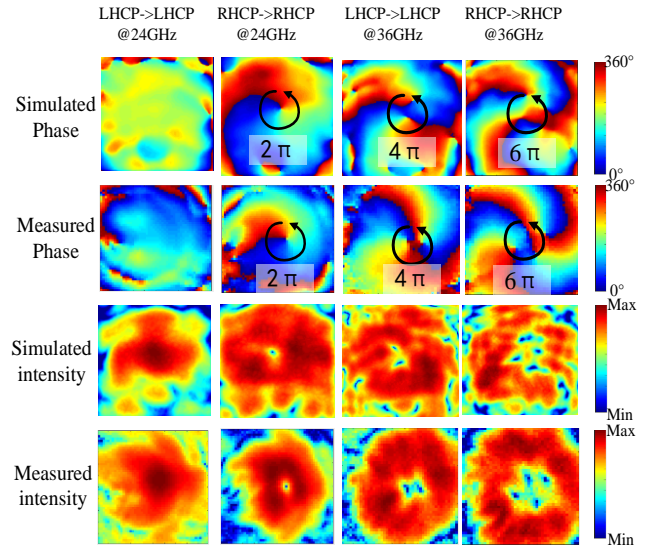where k is the free-space wavenumber. R_i is the distance from the feed phase center to the ith element. l is the topological charge number of OAM, and φ is the azimuthal angle around the beam axis. The OAM modes are selected as l=0 for the low-band LHCP channel, l=1 for the low-band RHCP channel, l=2 for the high-band LHCP channel, l=3 for the high-band RHCP channel. Therefore, the final required aperture phase can be obtained, as shown in Fig. 12. Then, based on the required aperture phase for the four different channels, we can calculate the corresponding dynamic phase and P-B phase. Specifically, the dynamic phase can be achieved by adjusting the size of the cross-bar structure and the P-B phase can be achieved by properly rotating the cross-bar structure for the high-band, as shown in Fig. 13 (a). As for the low-band, the dynamic phase is obtained by adjusting the length of TDLs and the P-B phase is obtained by rotating the circular patch and TDLs, as shown in Fig. 13 (b). Then, the corresponding MS can be designed, which consists of 18 ×18 UCs with an aperture size of 80mm×80mm.

Although the MS consists of five conductor layers with vias, it can be easily and conveniently fabricated using the conductor and dielectric joint 3-D printing technique with a single-layered compact form factor. The comprehensive, advanced 3-D printing system provides industrial-level around-the-clock printing of electronic circuitry. It prints electronic circuits and systems precisely by combining an exceptionally precise inkjet deposition printer with dedicated nano-inks. The printing resolution is 18μm along x- and y-direction and 10μm along z-direction. During the printing, a 0.75–1.4 μm near-infrared radiation (NIR) lamp and a 395 nm UV lamp are turned on to sinter the silver ink and cure the acrylate ink, respectively, with temperatures between 140°C to 170°C, as illustrated in Fig. 14. The printed sample is shown in Fig. 15. The 3-D printing technology is suitable for fabricating multi-layer structures with blind vias (e.g., more than 10 metal layers), which cannot be easily achieved using
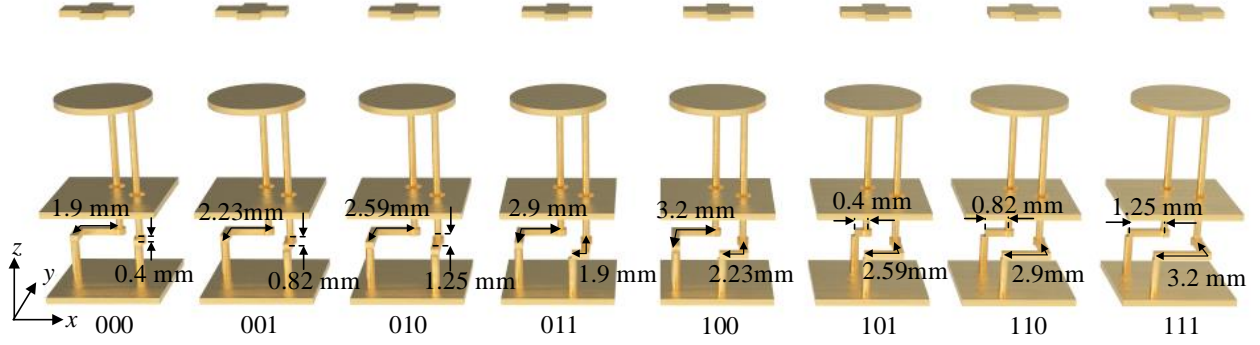
Fig.18. Eight-level UC with different lengths of TDLs to achieve low-band spin-decoupling with controllable EDR (Δφ=135°). (Not scaled in the z-direction)

conventional PCB technique. The printing time will not increase much when the number of layers increases since designs can be printed at one-stop. However, much more time will be used in multi-layer PCB fabrication since the bonding process takes additional time.

The sample is measured by a near-field measured system, as shown in Fig. 16. To reduce the blockage issue of the feed, the feed probe is offset at an angle of 23°. The loss due to the feed blockage is estimated to be around 0.3 dB. Considering the trade-off between the spillover efficiency, illumination efficiency and the illuminating angle at the edges, the feed position is optimized and the final value of θ_s (subtended angle between the maximum path and the minimum path) is finally selected as 56°. The MS covers the -10 dB edge taper of the feed, which is the typical value for edge taper [21]. The aperture efficiencies are 30% and 23% for the low-band and high-band, respectively, comparable to the state-of-the-art dual-band reflectarrays. The LHCP and RHCP probe are located 120 mm (*d*) away from the MS to record the intensity and phase. The distance (*d*) can be different values. Nevertheless, as the OAM beam is divergent, and the divergence of higher-order beams tends to be more significant than that of lower-order OAM beams, the scanning area must be sufficiently large for a very large distance to capture the magnitude and phase information for the OAM beams. In this regard, we choose a distance of 120 mm with 2500 pixels to capture the magnitude and phase information for all the higher-order OAM beams with acceptable measurement time. The simulated and measured near-field intensity and phase at 24 GHz and 36 GHz are shown in Fig. 17. The operating frequency band is from 23 GHz to 26 GHz for the low-band and from 35 GHz to 37 GHz for the high band. To directly observe the radiation performance versus operating frequency, we provide the supporting video where the performance of the MS can be directly viewed with frequency changes. As can be seen, the patterns will be gradually distorted when the frequency gradually shifts from central to edge frequencies.

III. METASURFACE FOR SPIN-DECOUPLED CHANNELS WITH CONTROLLABLE ENERGY DISTRIBUTION

This section will demonstrate that the energy distributions and wavefront in the co-polarization and cross-polarization can be independently controlled over dual-band by the proposed MS.

A. Principle and Meta-Atom Design

The Jones matrix of the reflective birefringent MS can be expressed as:

$$R = \begin{bmatrix} e^{j\delta_x} & 0 \\ 0 & e^{j\delta_y} \end{bmatrix} = e^{j\delta_x} \cdot \begin{bmatrix} 1 & 0 \\ 0 & e^{j\Delta\varphi} \end{bmatrix} \tag{12}$$

where Δφ is the reflection phase retardation along the *x*- and *y*-direction. When the meta-atom rotates with an angle of θ_g, the Jones matrix can be expressed as:

$$R(\theta_g) = S^{-1}(\theta_g) \cdot R \cdot S(\theta_g)$$

$$= \begin{bmatrix} \cos\theta_g & -\sin\theta_g \\ \sin\theta_g & \cos\theta_g \end{bmatrix} \cdot \begin{bmatrix} 1 & 0 \\ 0 & e^{j\Delta\varphi} \end{bmatrix} \begin{bmatrix} \cos\theta_g & \sin\theta_g \\ -\sin\theta_g & \cos\theta_g \end{bmatrix} \cdot e^{j\delta_x} \tag{13}$$

Considering the LHCP wave as the input, the output E-fields in the reflection space can be written as:

$$E_{out} = R(\theta_g) \cdot \begin{bmatrix} 1 \\ i \end{bmatrix} \cdot \frac{\sqrt{2}}{2}$$

$$= \frac{\sqrt{2}}{4}(1 + e^{i\Delta\varphi}) \cdot e^{i\delta_x} \cdot \begin{bmatrix} 1 \\ i \end{bmatrix} + \frac{\sqrt{2}}{4}(1 - e^{i\Delta\varphi}) \cdot e^{i\delta_x} \cdot e^{i\cdot 2\theta_g} \cdot \begin{bmatrix} 1 \\ -i \end{bmatrix}. \tag{14}$$

It is seen that energy distribution between the co-polarization and cross-polarization depends on the propagation phase retardation along fast and slow axes (*Δφ*). Meanwhile, the reflected RHCP phase solely depends on the dynamic phase (δ_x), and the reflected LHCP phase depends on the dynamic phase (δ_x) and P-B phase (rotation angle *θ*). This is understood that the P-B phase only exists with spin flips, *i.e.*, the LHCP incident wave to the reflected LHCP wave. The three parameters, i.e., *Δφ*, δ_x, and *θ* can be adjusted separately. Therefore, we can achieve the completely decoupled LHCP and RHCP channels with an arbitrarily controlled energy distribution ratio.

To evaluate the ratio of the power between the reflected co-polarization channel (LHCP) and cross-polarization channel (RHCP), we define the energy distribution ratio (EDR) as:

$$EDR = \frac{|1 - e^{j\cdot\Delta\varphi}|^2}{|1 + e^{j\cdot\Delta\varphi}|^2} = \tan^2(\frac{\Delta\varphi}{2}). \tag{15}$$
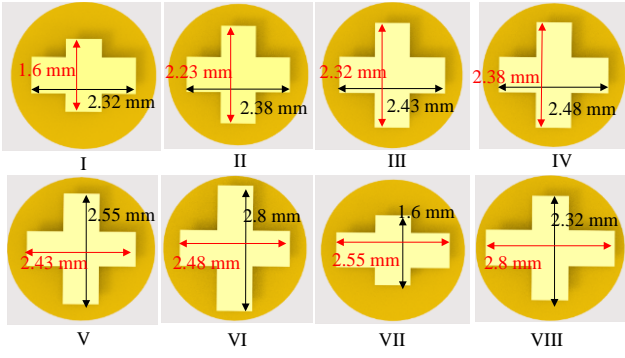
Fig.19. Configuration of the eight-level cross-bar structure for high-band spin-decoupling with controllable EDR. ($\Delta\varphi$=90°)
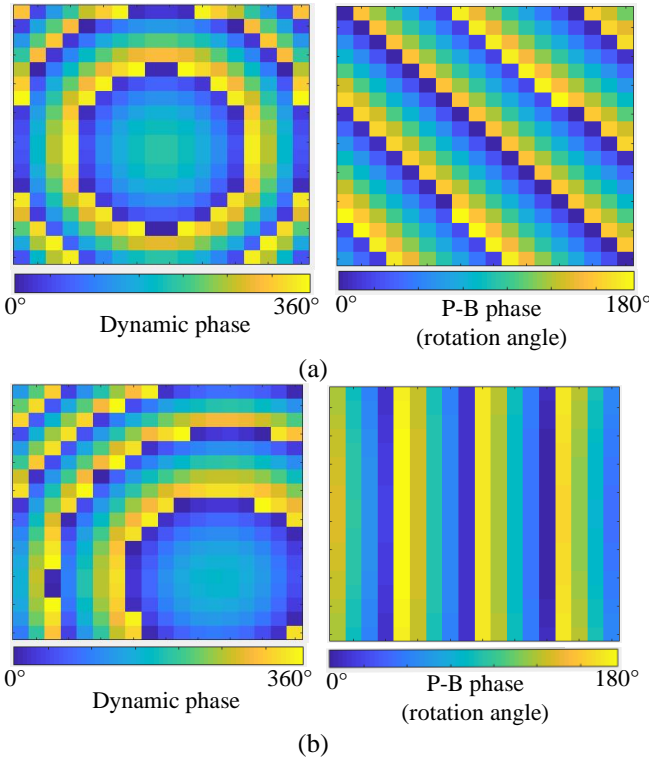

Fig.20. (a) Phase masks for high-band. (b) Phase masks for low-band.

The value of the EDR can be from zero to infinite depending on the propagation phase retardation along fast and slow axes ($\Delta\varphi$). Note that the $\Delta\varphi$ is equal to 180° for both bands in Section II. Therefore, all energy exists in the reflected co-polarization channel. Here, the $\Delta\varphi$ is set as 90° and 135° for the high-band and low-band, respectively. Hence, the EDRs are 1 and 5.83 for the high-band and low-band, respectively. The corresponding dimensions of the UC for the low-band and high-band are given in Figs. 18 and 19, respectively.

B.   MS Design and Results

The MS is designed to collimate the EM-wave from the feed and focus on different positions for the LHCP and RHCP incident waves in low-band and high-band, respectively. Specifically, the focal points are set as (40mm, 0mm, 120mm), (0mm, -40mm, 120mm), (0mm, -40mm, 120mm), and (0mm,

40mm, 120mm) for the co-polarization and cross-polarization channels in the high-band and low-band, respectively. The phase profile of R_{LL}, R_{RL} for the low-band and high-band can be respectively expressed as:

$$R_{LL}(x, y) = k \cdot R_i + k \cdot R_{LLi-low} \quad \text{for low-band (16)}$$

$$R_{RL}(x, y) = k \cdot R_i + k \cdot R_{RLi-low} \quad \text{for low-band (17)}$$

$$R_{LL}(x, y) = k \cdot R_i + k \cdot R_{LLi-high} \quad \text{for high-band (18)}$$

$$R_{RL}(x, y) = k \cdot R_i + k \cdot R_{RLi-high} \quad \text{for high-band (19)}$$

where $R_{LLi-low}$ and $R_{RLi-low}$ represent the focal point to the ith element for the reflected LHCP and RHCP channels under the LHCP incident wave in the low-band. $R_{LLi-high}$ and $R_{RLi-high}$ represent the focal point to the ith element for the reflected LHCP and RHCP channels under the LHCP incident wave in the high-band.

Based on the equations (12) to (19), the corresponding dynamic and P-B phase masks for low-band and high-band are given in Fig. 20. The printed sample is shown in Fig. 21. The simulated and measured near-field intensity at 25 GHz and 36 GHz are shown in Fig. 22. It is seen that the reflected energy is near equally distributed in co-polarization and cross-polarization at 36 GHz under LHCP incident wave, while most of the energy is focused in the reflected co-polarization channel and only a small portion is located in cross-polarization channel at 25 GHz.

Table I compares the key features of the proposed work with state-of-the-art dual-band spin-decoupled MSs. Interleaving two different structures, with each operating at a single frequency band, is a convenient approach to achieve dual-band spin-decoupling with small lateral sizes [35],[36]. Nevertheless, the periods of the UC are usually large, which might affect the MS performance, such as beam scanning angle. Stacking UCs into different layers with FSS ensures a small period with low mutual interference [39],[40]. However, the designs require multiple PCB layers with large lateral size. The proposed non-interleaved UC features a small period and low mutual interference. The multi-layered configuration can be fast-prototyped in a single-layer substrate. However, it is also worth mentioning that because the phase-shifting depends on the resonance, achieving the broadband spin decoupled beam-shaping is difficult for the current design. More specifically, the high-band phase-shifting is based on the
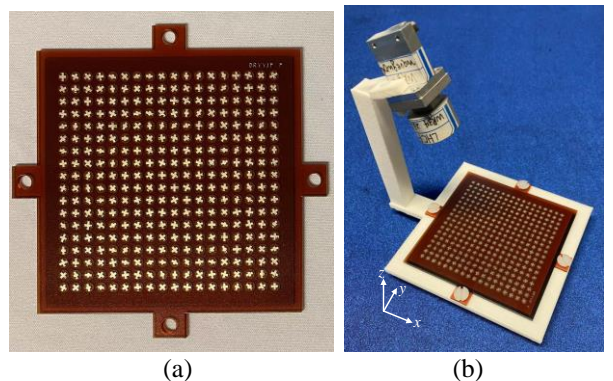

Fig. 21. (a) Top view of the MS. (b) Assembling view of the MS.

TABLE I
COMPARISON OF THE STATE-OF-THE-ART DUAL-BAND SPIN DECOUPLED REFLECTIVE MS

| Ref.	Freq (GHz)	Configuration	UC size (Compare with wavelength)	Resolution	Function	Fabrication
[37]	8/13	Interleaved	20mm (0.6/0.8)	---	Spatial multiplexed OAM and hologram	PCB
[38]	20/30	Interleaved	6mm (0.4/0.6)	3-bit	Collimating reflectarray	PCB
[39]	12/29	Multi-layer UC + FSS	10mm/5mm (0.4/0.484)	3-bit	OAM	PCB
[40]	12/29	Multi-layer UC + FSS	10mm/5mm (0.4/0.484)	3-bit	Collimating reflectarray	PCB
[41]	12/22	Dual-layer UC	6mm (0.24/0.44)	1-bit	Hologram	PCB
This work	25/36	Multi-layer UC	4mm (0.33/0.48)	3-bit	OAM	3-D printing
				3-bit	Focusing (controlled energy distribution)	
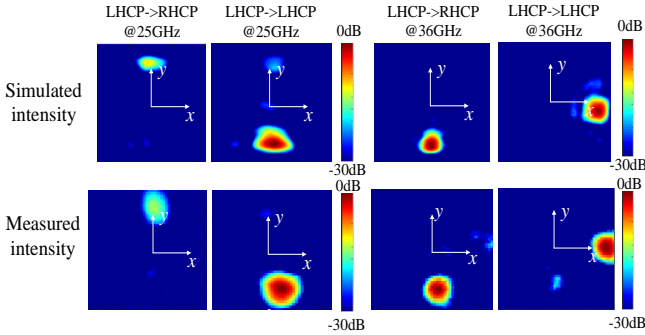
Fig. 22. Simulated and measured near-field intensity.

cross-bar's resonance. As for the low band, although the phase-shifting depends on the length of strip lines (less dispersive), the circular-shaped patch antenna is still based on resonance. Therefore, the operating bandwidth cannot be sufficiently wide due to its resonant nature. Improving the bandwidth over dual-band will be valuable future work.

IV. CONCLUSION

In summary, 3-D printed non-interleaved reflective MSs supporting mm-wave dual-band spin-decoupled quadruplex channels with independent beam-shaping were demonstrated. In addition, it is also demonstrated that the energy distributions and wavefront in the co-polarization and cross-polarization can be independently controlled in dual-band by the proposed MS. The strategy will find broader applications in the future reconfigurable intelligent surfaces (RIS) system if the energy distributions can be dynamically controlled.

V. ACKNOWLEDGMENT

REFERENCES

[1] F. Aieta, M. Kats, P. Genevet, F. Capasso, " Multiwavelength achromatic metasurfaces by dispersive phase compensation," *Science*, 347, 6228, Feb. 2015.

[2] N. Yu, P. Genevet, M. A. Kats, F. Aieta, J.-P. Tetienne, F. Capasso, Z. Gaburro, "Light propagation with phase discontinuities: generalized laws of reflection and refraction, " *Science*, 334, 333, Sep. 2011.

[3] J. Y. Dai *et al.*, "Wireless communication based on information metasurfaces," *IEEE Trans. Microw. Theory Techn.*, vol. 69, no. 3, pp. 1493-1510, Mar. 2021.

[4] F. Qin, L. Ding, L. Zhang, F. Monticone, C. C. Chum, J. Deng, S. Mei, Y. Li, J. Teng, M. Hong, S. Zhang, A. Alù, C. W. Qiu, "Hybrid bilayer plasmonic metasurface efficiently manipulates visible light," *Sci. Adv.*, 2, e1501168, Jan. 2016.

[5] J. Wang *et al*., "Metantenna: when metasurface meets antenna again, " *IEEE Trans. Antennas Propag*., vol. 68, no. 3, pp. 1332-1347, Mar. 2020.

[6] L. Li, P. Zhang, F. Cheng, M. Chang, and T. J. Cui, "An optically transparent near-field focusing metasurface," *IEEE Trans. Microw. Theory Techn.*, vol. 69, no. 4, pp. 2015-2027, Apr. 2021.

[7] G. B. Wu, S. Y. Zhu, S. W. Pang, and C.H. Chan. "Superheterodyne-inspired waveguide-integrated metasurfaces for flexible free-space light manipulation, " *Nanophotonics*, 11(20): 4499-4514, Sep. 2022.

[8] G. B. Wu, J. Y. Dai, Q. Cheng, T. J. Cui, and C.H. Chan. "Sideband-free space–time-coding metasurface antennas," *Nat Electron* 5, 808–819, Nov. 2022.

[9] Y. Wang et al., "Broadband high-efficiency ultrathin metasurfaces with simultaneous independent control of transmission and reflection amplitudes and phases," *IEEE Trans. Microw. Theory Techn.*, vol. 70, no. 1, pp. 254-263, Jan. 2022.

[10] J. Zhu, Y. Yang, M. Li, D. McGloin, S. Liao, J. Nulman, F. Iacopi, "Additively manufactured millimeter-wave dual-band single-polarization shared aperture Fresnel zone plate metalens antenna," *IEEE Trans. Antennas Propag*., vol. 69, no. 10, pp. 6261-6272, Oct. 2021.

[11] K. Zhang, Y. Wang, S. N. Burokur and Q. Wu, "Generating dual-polarized vortex beam by detour phase: from phase gradient metasurfaces to metagratings," *IEEE Trans. Microw. Theory Techn.*, vol. 70, no. 1, pp. 200-209, Jan. 2022.

[12] G. Valerio, F. Ghasemifard, Z. Sipus and O. Quevedo-Teruel, "Glide-symmetric all-metal holey metasurfaces for low-dispersive artificial materials: modeling and properties," *IEEE Trans. Microw. Theory Techn.*, vol. 66, no. 7, pp. 3210-3223, Jul. 2018.

[13] M. Afzal, K. Esselle, "Steering the beam of medium-to-high gain antennas using near-field phase transformation," *IEEE Trans. Antennas Propag*., 65(4): 1680-1690, 2017.

[14] B. Orazbayev, N. M. Estakhri, A. Alù, M. Beruete, "Experimental demonstration of metasurface-based ultrathin carpet cloaks for millimeter waves, " *Adv. Opt. Mater.*, 5, 1600606, Nov.2017.

[15] Q. Zhao and C. D. Sarris, "Space–time adaptive modeling and shape optimization of microwave structures with applications to metasurface design," *IEEE Trans. Microw. Theory Techn.*, vol. 70, no. 12, pp. 5440-5453, Dec. 2022.

[16] H. T. Chen, A. J. Taylor, N. Yu, "A review of metasurfaces: physics and applications. " *Rep. Prog. Phys*, 79(7): 076401, Jun. 2016.

[17] M. F. Imani *et al*., "Review of metasurface antennas for computational microwave imaging, " *IEEE Trans. Antennas Propag.*, 68(3): 1860-1875, 2020.

[18] F. Ding, A. Pors, S I. Bozhevolnyi, "Gradient metasurfaces: a review of fundamentals and applications, " *Rep. Prog. Phys*, 81(2): 026401, Aug, 2017,

[19] M. R. Akram, G. Ding, K. Chen, Y. Feng, W. Zhu, "Ultrathin single layer metasurfaces with ultra-wideband operation for both transmission and reflection, " *Adv. Mater*, 32(12): 1907308, Feb. 2020.

[20] M. Tymchenko, et al. "Gradient nonlinear pancharatnam-berry metasurfaces." *Phys. Rev. Lett* 115.20 : 207403, Nov.2015.

[21] P. Nayeri, F. Yang, and A. Z. Elsherbeni, *Reflectarray Antennas: Theory, Designs, and Applications*. Hoboken, NJ, USA: Wiley, 2018.

[22] J. Zhu, S. Liao and Q. Xue, "3-D printed millimeter-wave metal-only dual-band circularly polarized reflectarray," *IEEE Trans. Antennas Propag.*, vol. 70, no. 10, pp. 9357-9364, Oct. 2022.

[23] R. Xie, G. Zhai, X. Wang, D. Zhang, L. Si, H. Zhang, J. Ding, "High efficiency ultrathin dual wavelength pancharatnam berry metasurfaces with complete independent phase control, " *Adv. Opt. Mater*., 7(20), 1900594, Jul. 2019.

[24] Y. Guo, S. Zhang, M. Pu, Q. He, J. Jin, M. Xu, Y. Zhang, P. Gao, X. Luo, "Spin-decoupled metasurface for simultaneous detection of spin and orbital angular momenta via momentum transformation, " *Light: Sci. Appl*., 10(1), 63, Mar. 2021.

[25] H. Xu, L. Han, Y. Li, Y. Sun, J. Zhao, S. Zhang, C.-W. Qiu, "Completely spin-decoupled dual-phase hybrid metasurfaces for arbitrary wavefront control, " *ACS Photonics*, 6, 211, Jan. 2019.

[26] H. Xu, C. Wang, G. Hu, Y. Wang, S. Tang, Y. Huang, X. Ling, W. Huang, and C. Qiu, " Spin-encoded wavelength-direction multitasking Janus metasurfaces, " *Adv. Opt. Mater*.,9(11), 2100190, May, 2021.

[27] Z. Jiang, F. Wu, T. Yue, W. Hong, " Wideband and low-profile integrated dual-circularly-polarized transmit-arrays enabled by antenna-filter-antenna phase shifting cells," *IEEE Trans. Antennas Propag*, 69(11), 7462-7475, 2021.

[28] Z. Li, D. Zhang, J. Liu, J. Zhang, L. Shao, X. Wang, R. Jin, and W. Zhu, " 3-D manipulation of dual-helical electromagnetic wavefronts with a non-interleaved metasurface", *IEEE Trans. Antennas Propag*., 70(1), 378–388, 2022.

[29] Y. Yuan, Q. Wu, S.N. Burokur, and K.Zhang, "Chirality-assisted phase metasurface for circular polarization preservation and independent hologram imaging in microwave region," *IEEE Trans. Microw. Theory Techn*, early access, 2023.

[30] Z. X. Wang, J. W. Wu, L. W. Wu, Y. Gou, H. F. Ma, Q. Cheng, and T. J. Cui, "High efficiency polarization encoded holograms with ultrathin bilayer spin-decoupled information metasurfaces, " *Adv. Opt. Mater*., 9(5), 2001609, Jan. 2021.

[31] Y. Yuan, K. Zhang, X. Ding, B. Ratni, S. N. Burokur, Q. Wu, "Complementary transmissive ultra-thin meta-deflectors for broadband polarization-independent refractions in the microwave region "*Photonics Res*. 7, Jun. 2019,

[32] Y. Xu, H. Zhang, Q. Li, X. Zhang, Q. Xu, W. Zhang, C. Hu, X. Zhang, J. Han, W. Zhang, "Generation of terahertz vector beams using dielectric metasurfaces via spin-decoupled phase control, " *Nanophotonics*, 9, 3393, Sep. 2020.

[33] K. Zhang, Y. Yuan, X. Ding, B. Ratni, S. N. Burokur, Q. Wu. "High-efficiency metalenses with switchable functionalities in microwave region, " *ACS Appl. Mater. Interfaces*, 11, 28423-28430, Jun. 2019.

[34] G. Ding, K. Chen, G. Qian, J. Zhao, T. Jiang, Y. Feng, Z. Wang "Independent energy allocation of dual helical multi-beams with spin-selective transmissive metasurface," *Adv. Opt. Mater.*, 8(16): 2000342, May. 2020.

[35] J. C. Ke, et al. "Space-frequency-polarization-division multiplexed wireless communication system using anisotropic space-time-coding digital metasurface. " *Natl. Sci. Rev*, 9(11): nwac225. Oct. 2022,

[36] L. Zhang, et al. "A wireless communication scheme based on space- and frequency-division multiplexing using digital metasurfaces, " *Nat Electron* 4, 218–227, May, 2021.

[37] H.-X. Xu, G. Hu, M. Jiang, Y. W. S. Tang, Z. Wang, Y. Huang, X. Ling, H. Liu, J. Zhou, "Wavevector and frequency multiplexing performed by a spin-decoupled multichannel metasurface, " *Adv. Mater. Technol*., 5(1): 1900710, Jan. 2020.

[38] X. Tong, Z. H. Jiang, Y. Li, F. Wu, R. Sauleau and W. Hong, "Dual-wideband dual-circularly-polarized shared-aperture reflectarrays with a single functional substrate for K-/Ka-Band applications," *IEEE Trans. Antennas Propag*, vol. 70, no. 7, pp. 5404-5417, July 2022.

[39] P. Xu, H. Liu, R. Li, K. Zhang and L. Li, "Dual-band spin-decoupled metasurface for generating multiple coaxial OAM beams," *IEEE Trans. Antennas Propag*, vol. 70, no. 11, pp. 10678-10690, Nov. 2022.

[40] P. Xu, L. Li, R. Li and H. Liu, "Dual-circularly polarized spin-decoupled reflectarray with FSS-back for independent operating at Ku-/Ka-bands," *IEEE Trans. Antennas Propag*, vol. 69, no. 10, pp. 7041-7046, Oct. 2021.

[41] Y. Gou, H. F. Ma, L.W. Wu, et al. "Non-interleaved polarization-frequency multiplexing metasurface for multichannel holography, " *Adv. Opt. Mater*., 2201142, Aug. 2022.

[42] Y. Yuan, S. Sun, Y. Chen, K. Zhang, X. Ding, B. Ratni, Q. Wu, S. Burokur, C. Qiu, "A fully phase-modulated metasurface as an energy-controllable circular polarization router, " *Adv. Sci.* 7, 2001437, Sep. 2020.

[43] J. Zhu, Y. Yang, N. Hu, S. Liao, J. Nulman, "Additively manufactured multi-material ultrathin metasurfaces for broadband circular polarization decoupled beams and orbital angular momentum generation." *ACS Appl. Mater. Interfaces* 13.49 59460-59470, Dec. 2021.

[44] J. Zhu, Y. Yang, F. Wang, J. Lai, and M. Li, "3D printed spin decoupled transmissive metasurfaces based on versatile broadband cross-polarization rotation meta-atom," *Adv. Opt. Mater*., vol. 11, no. 4, Feb. 2023.

Jianfeng Zhu (Member, IEEE) was born in Hunan, China. He received the B. Eng. degree in communication engineering from Beijing University of Posts and Telecommunications (BUPT), Beijing, China and Ph. D. degree from BUPT and University of Technology Sydney (UTS), Ultimo, NSW, Australia. He is now with South China University of Technology. His research interests include millimeter-wave and terahertz antennas and metasurfaces. He is looking for collaborators.
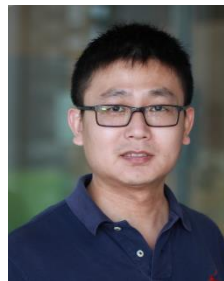
Yang Yang (Senior Member, IEEE) was born in Bayan Nur, Inner Mongolia, China and received the PhD degree in Electronic Engineering from Department of Electrical and Computer Systems Engineering, Monash University, Melbourne, Australia, in 2013.
Dr Yang was with the State Key Laboratory of Terahertz and Millimeter Waves, City University of Hong Kong, in 2016. Since December 2016, he joined the University of Technology Sydney (UTS), Australia. He is currently an Associate Professor and a Group Leader of 3D Millimetre-Wave and Terahertz Circuits and Antennas in UTS Tech Lab. His research interests include emerging RF materials and additive manufacturing techniques for 3D millimetre-wave

and terahertz device designs for 5G and biomedical applications. He has over 200 international publications in microwave, millimetre-wave and terahertz circuits and antennas. In 2021, Dr Yang received the Linkage Infrastructure, Equipment and Facilities (LIEF) Award funded by the Australian Research Council to establish the national laboratory of Australian 3D Terahertz Beam Measurement Platform (500 GHz). Dr Yang is a current Associate Editor of *IEEE Transactions on Microwave Theory and Techniques* (from 2022). He is the Chair of IEEE MTT-S Education Resources Development (2023), and Chair of IEEE NSW AP-S/MTT-S Joint Chapter (2023).

Jiexin Lai was born in Guangdong, China, in 1993. He received the B.S. and M.S. degrees from Shenzhen University, Shenzhen, China, in 2016 and 2020, respectively. He is currently pursuing the Ph.D. degree with the University of Technology Sydney, Ultimo, NSW, Australia. His research interests include wideband antenna, indoor antenna, metasurface, millimeter-wave and terahertz wave.

Mengze Li (Student Member, IEEE) was born in Hunan, China, in 1994. She received the B.Eng. degree in electrical engineering and automation from Hunan University, Hunan, in 2015, and the M.Eng. degree in electronic field and microwave technology from Xiamen University, Xiamen, China, in 2018. and she received the Ph.D. degree with the Faculty of Engineering and Information Technology, University of Technology Sydney, Australia. From 2017 to 2018, she was a Visiting Student with the Faculty of Engineering and Information Technology, University of Technology Sydney.
Her current research interests include microstrip filters, multiplexers, power divider, RFIC, reflectarrays, LTCC technology, and 3-D printing technology.